Unpolarized infrared emissivity with shadow from anisotropic rough sea surfaces with non-Gaussian statistics

Christophe Bourlier

The emissivity of two-dimensional anisotropic rough sea surfaces with non-Gaussian statistics is investigated. The emissivity derivation is of importance for retrieval of the sea-surface temperature or equivalent temperature of a rough sea surface by infrared thermal imaging. The well-known Cox–Munk slope probability-density function, considered non-Gaussian, is used for the emissivity derivation, in which the skewness and the kurtosis (related to the third- and fourth-order statistics, respectively) are included. The shadowing effect, which is significant for grazing angles, is also taken into account. The geometric optics approximation is assumed to be valid, which means that the rough surface is modeled as a collection of facets reflecting locally the light in the specular direction. In addition, multiple reflections are ignored. Numerical results of the emissivity are presented for Gaussian and non-Gaussian statistics, for moderate wind speeds, for near-infrared wavelengths, for emission angles ranging from 0° (nadir) to 90° (horizon), and according to the wind direction. In addition, the emissivity is compared with both measurements and a Monte Carlo ray-tracing method.

OCIS codes: 290.5880, 000.5490, 010.4450, 260.3060, 280.0280.

1. Introduction

The emissivity of the ocean surface in atmospheric transmission windows is an important parameter for retrieving the sea-surface temperature (SST) from radiometric sensors located either on satellites or on platforms close to the sea's surface. It has been established that, for an accuracy of 0.3 K in SST retrieval, the error in the emissivity must be approximately 0.5%.[1] Consequently, the sea-surface emissivity needs to be determined with accuracy. In most SST retrieval algorithms the sea-surface emissivity is assumed to be a constant (e.g., 0.98), explicitly or implicitly. This assumption has been verified for emission angles close to zero (typically smaller than 30°–40°), and it may be used for a camera located on a satellite platform. But, for infrared systems at low altitudes, i.e., for emission angles greater than 60°, the emissivity depends on the emission angle, on the wind direction, and on the wind speed.

Emissivity models developed in Refs. 1–4 neglected the dependence on wind direction (isotropic surface) and ignored the shadowing effect, whereas in Refs. 5 and 6 the surface was assumed to be one dimensional and the shadowing effect was included. The model presented in this paper is based on Refs. 7–9, in which a two-dimensional rough sea surface with Gaussian statistics is considered and in which the shadowing effect is taken into account. Nevertheless, unlike in Ref. 7, Bourlier *et al.*[8,9] made no assumption in the derivation of the two-dimensional shadowing function. As presented in Refs. 10–12, the emissivity can be also derived from the hemispheric reflectivity, for which the sea surface is assumed to be Gaussian and anisotropic and the shadowing effect is ignored, unlike in Ref. 9. The hemispheric reflectivity is obtained from integration of the reflectivity over the half-space above the sea surface. In the research reported in this paper this technique was not used because the formulation is more complicated and the surface reflectivity is needed only for the calculation of sun glint. Indeed, as shown in Refs. 9–11, by using the radiative transfer method one can calculate the thermal radiation received by the infrared sensor, which depends on the atmospheric transmission coefficient, on the surface reflectivity, and on the sur-

The author (christophe.bourlier@univ-nantes.fr) is with the Radar Team, Institut de Recherche en Electrotechnique et Electronique de Nantes Atlantique, Ecole Polytechnique de l'Université de Nantes, Rue Christian Pauc, La Chantrerie, B. P. 50609, 44306 Nantes Cedex 3, France.

Received 9 July 2004; revised manuscript received 17 December 2004; accepted 27 December 2004.

0003-6935/05/204335-15$15.00/0

face emissivity. In this paper we shall focus only on the intrinsic radiation of the sea surface related to its emissivity.

All quoted references assume Gaussian statistics of the surface slopes given by the Cox–Munk[13] slope probability-density function (PDF) truncated up to the second-order statistics. Indeed, the contributions of the third- (related to the skewness) and the fourth- (related to the kurtosis) order statistics are ignored. In this paper the higher-order statistics are included in the calculations of the shadowing function and of the emissivity. Comparisons of Gaussian and non-Gaussian statistics are presented for wavelengths of 4 and 10 μm, for moderate wind speeds, for emission angles ranging from 0° (nadir) to 90° (horizon), and for wind directions ranging from 0° (upwind direction) to 360°.

Before proceeding, one can note that this study of the rough sea-surface emissivity is governed by several assumptions and approximations. In particular, the sea surface is assumed to be opaque for the infrared wavelengths studied. The sea surface is modeled as being single valued and composed of a continuous collection of smooth facets with continuous first derivatives between adjacent facets. Each facet is assumed to be large with respect to the wavelength of radiation, and geometrical optics is assumed to be a valid approximation for describing the interaction of radiation with any given facet. Contributions from multiple reflections are not included in the model (comparisons with a Monte Carlo ray-tracing method will show that multiple reflections can be omitted for emission angles smaller than 60° and that the difference between the emissivity with single reflection and the emissivity computed with multiple reflections cannot exceed 0.03). Atmospheric effects such as transmission loss and refraction are completely ignored. Electromagnetic radiation is taken to be unpolarized. In addition, we use the Cox–Munk slope PDF, which is valid for near-neutral stability conditions (the air and sea temperatures are equal) and for emission angles smaller than 35°. The dependence of the sea's roughness on the stability has been described by Hwang and Shemdin[14] and by Wu.[15] The specific discussion by Shaw and Churnside of a stability correction for the Cox–Munk PDF is reported in Ref. 16. They used measurements made with a laser glint meter and a micrometer-wave radiometer for determining stability (wherein it was shown that the Cox–Munk model requires a stability correction when the air and the water temperatures differ by even a few tenths of a degree).

The paper is organized as follows: In Section 2 the shadowing function is presented, and in Section 3 we derive the emissivity by taking the shadowing effect into account. Numerical results of the emissivity, and comparison with measurements,[17,18] are presented, together with the Monte Carlo ray-tracing method.[19] The final section gives concluding remarks.

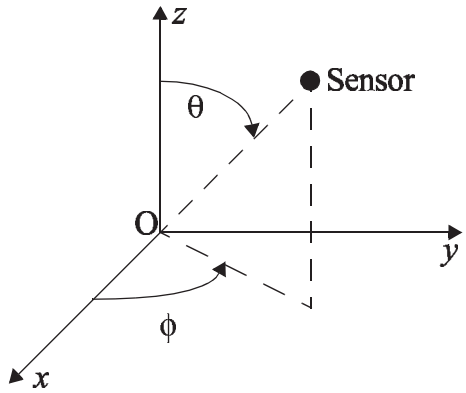

Fig. 1. Coordinate system used to derive the shadowing function and the emissivity. θ is the emission angle defined with respect to (*Oz*), and ϕ is the wind direction defined in the plane (*Ox, Oy*).

2. Shadowing Function

The emission angle with respect to the nadir of the sensor is denoted θ, and the azimuthal direction of the sensor with respect to the upwind direction (see Fig. 1) is denoted ϕ. θ = 0 gives the nadir, whereas θ = 90° gives the horizon (grazing angle). {ϕ = 0°, 90°, 180°} correspond to the upwind, crosswind, and downwind directions, respectively (see Fig. 2). The shadowing function is defined as the ratio of the surface seen by the receiver to the total surface (see Fig. 3).

A. Derivation of the Shadowing Function

The problem of wave scattering from a rough surface in the presence of shadowing was first considered analytically in Ref. 20 and Chap. 7 of Ref. 21 by means of the theory of random function overshoots developed in Ref. 22. The statistical (this means that the averaging over the surface slopes and heights is not performed) shadowing function was then expressed from an infinite Rice series (for more details, see Ref. 23). The shadowing effect was rediscovered later, seemingly independently, with the Wagner,[24] Smith,[25,26] and Beckman[27] formulations, which retained the first term of the series. Moreover, Smith

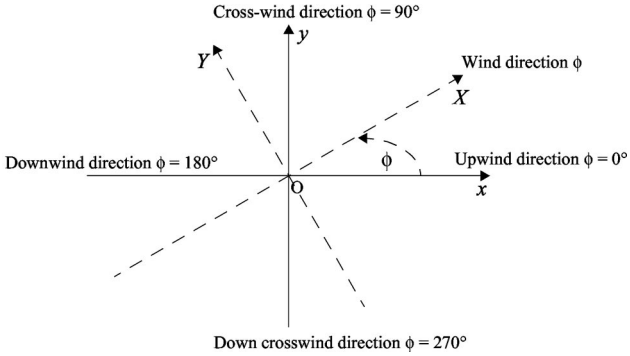

Fig. 2. Illustration of the basis used to calculate the marginal slope PDF. The surface slopes $\{\gamma_X, \gamma_Y\}$ defined in basis (*OX, OY*) are obtained from surface slopes $\{\gamma_x, \gamma_y\}$ defined in basis (*OX, OY*), by rotation of angle ϕ, where ϕ is the wind direction.

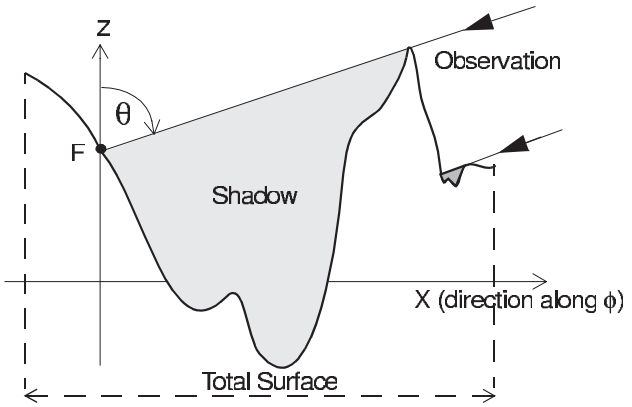

Fig. 3. Definition of the shadowing function F is an arbitrary point on the surface of height z and of slopes $\{\gamma_x, \gamma_y\}$ defined in basis (OX, OY) (see Fig. 2).

used the Wagner approach by introducing a normalization function. For monostatic and bistatic configurations those authors assumed a one-dimensional surface with an uncorrelated Gaussian process of surface heights and slopes. This means that the statistical shadowing function is independent of the surface correlation function. Recently, to analyze the correlation effect, for one- and two-dimensional surfaces with a correlated Gaussian process of the surface heights and slopes Bourlier *et al.*[23] and Bourlier and Berginc[28] showed that the correlation can be neglected. Moreover, comparisons of the Wagner and the Smith shadowing functions with numerical results computed from Ref. 29 showed that the Smith approach is more accurate than the Wagner one. Thus in this paper the Smith statistical uncorrelated shadowing function, $S(\theta, \phi|\gamma_X, z)$ is applied.

For a monostatic configuration, it is expressed as (for more details see Ref. 23)

$$S(\theta,\ \phi|\gamma_X; z) = \Upsilon(\mu - \gamma_X) \times [P_h(z) - P_h(-\infty)]^{\Lambda(\theta,\ \phi)}, \tag{1}$$

where

$$P_h(z) = \int p_h(z)\mathrm{d}z,$$

$$\Lambda(\theta,\ \phi) = \frac{1}{\mu}\int_{\mu}^{\infty} (\gamma_X - \mu)p_s(\gamma_X)\mathrm{d}\gamma_X, \quad \mu = \cot\theta. \tag{2}$$

In the above equations, $P_h(z)$ is a primitive of the surface height PDF, $p_h(z)$, where z is the height of an arbitrary point on the surface. μ denotes the slope of the incident beam along the wind direction, ϕ. $\Upsilon(x)$ is a unit step function, defined as $\Upsilon(x) = 1$ if $x \geq 0$, and 0 else. In addition, the slope marginal probability, $p_s(\gamma_X)$, is expressed as

$$p_s(\gamma_X) = \int_{-\infty}^{+\infty} p_s(\gamma_X,\ \gamma_Y)\mathrm{d}\gamma_Y, \tag{3}$$

where $\{\gamma_X, \gamma_Y\}$ are the surface slopes along the ϕ direction and the orthogonal direction, respectively. The slopes $\{\gamma_x, \gamma_y\}$ are obtained from $\{\gamma_X, \gamma_Y\}$ by rotation of an angle $-\phi$ (Fig. 2):

$$\begin{aligned}\gamma_x &= \gamma_X \cos\phi - \gamma_X \sin\phi,\\ \gamma_y &= \gamma_X \sin\phi + \gamma_Y \cos\phi.\end{aligned} \tag{4}$$

Equation (1) shows that the shadowing function carries a restriction over the surface slopes, within the Υ function (only surface slopes γ_X smaller than μ are taken into account), and modifies the height PDF, $p_h(z)$, that is due to the term $[P_h(z) - P_h(-\infty)]^{\Lambda}$.

Inasmuch as the emissivity does not depend on elevation z (see section 3 below), we can average over height z, leading to

$$\begin{aligned}S(\theta,\ \phi\,|\,\gamma_X) &= \int_{-\infty}^{+\infty} S(\theta,\ \phi\,|\,\gamma_X,\ z) \times p_h(z)\mathrm{d}z\\ &= \frac{\Upsilon(\mu - \gamma_X)}{\Lambda + 1}\end{aligned} \tag{5}$$

for any p_h.

B. Application to Gaussian and Non-Gaussian Statistics

Here we apply Eq. (5), valid for any surface statistics, to Gaussian and non-Gaussian statistics by considering the Cox–Munk slope PDF.[13]

1. Cox–Munk Slope PDF

The Cox–Munk experimental slope PDF is given by successive sums of Gram–Charlier series truncated up to fourth order. It is expressed as

$$\begin{aligned}p_s(\gamma_x,\ \gamma_y) = \frac{1}{2\pi\sigma_{sx}\sigma_{sy}} \exp\left(-\frac{{\gamma_x}^2}{2{\sigma_{sx}}^2} - \frac{{\gamma_y}^2}{2{\sigma_{sy}}^2}\right)\Bigg[1 + \frac{c_{21}}{2}\\ \times ({\Gamma_y}^2 - 1)\Gamma_x + \frac{c_{03}}{6}({\Gamma_x}^2 - 3)\Gamma_x + \frac{c_{22}}{4}\\ \times ({\Gamma_x}^2 - 1)({\Gamma_y}^2 - 1) + \frac{c_{40}}{24}({\Gamma_y}^4 - 6{\Gamma_y}^2 + 3)\\ + \frac{c_{04}}{24}({\Gamma_x}^4 - 6{\Gamma_x}^2 + 3)\Bigg],\end{aligned} \tag{6}$$

where

$$\Gamma_{x,y} = \frac{\gamma_{x,y}}{\sigma_{sx,\,sy}}, \qquad {\sigma_{sx}}^2 = (3.16u_{12} \pm 4)10^{-3},$$

$${\sigma_{sy}}^2 = (1.92u_{12} + 3 \pm 4)10^{-3}, \tag{7}$$

$$\begin{aligned}c_{21} &= (0.86u_{12} - 1 \pm 3)10^{-2} \geq 0,\\ c_{03} &= (3.3u_{12} - 4 \pm 12)10^{-2} \geq 0;\\ c_{04} &= 0.23 \pm 0.41,\\ c_{40} &= 0.40 \pm 0.23,\\ c_{22} &= 0.12 \pm 0.06.\end{aligned} \tag{8}$$

Here + or − indicates the measurement error. In relations (7) and (8) parameter u_{12} is the wind speed at 12.5 m above the sea surface. In Eq. (6), and $\{c_{21}, c_{03}\}$ are related to the third-order statistics, whereas $\{c_{22}, c_{04}, c_{40}\}$ are related to the fourth-order statistics. When these coefficients vanish, the slope's PDF is Gaussian. Our purpose in this paper is to study the effect of the third- and fourth-order statistics on the shadowing function and on the emissivity.

2. Derivation of the Marginal Probability

The determination of Λ, given by Eqs. (2), requires the calculation of the marginal slope probability $p_s(\gamma_X)$ defined by Eqs. (3) and (4). Substituting Eq. (6) into Eq. (3), after simple but tedious manipulations, we show that

$$p_s(\gamma_X) = \frac{1}{\sigma_{sX}\sqrt{2\pi}} \exp\left(-\frac{\gamma_X^2}{2\sigma_{sX}^2}\right)\left[1 + \alpha_K\left(1 - 2\frac{\gamma_X^2}{\sigma_{sX}^2} + \frac{\gamma_X^4}{3\sigma_{sX}^4}\right) + \alpha_S\left(\frac{\gamma_X}{\sigma_{sX}} - \frac{\gamma_X^3}{3\sigma_{sX}^3}\right)\right], \tag{9}$$

where

$$\alpha_S(\phi) = -\frac{\sigma_{sx}\cos\phi}{2\sigma_{sX}^3}[c_{03}(\sigma_{sx}\cos\phi)^2 + 3c_{21}(\sigma_{sy}\sin\phi)^2], \tag{10}$$

$$\alpha_K(\phi) = \frac{1}{8\sigma_{sX}^4}\left[c_{04}(\sigma_{sx}\cos\phi)^4 + c_{40}(\sigma_{sy}\sin\phi)^4 + \frac{3}{2}c_{22}\sigma_{sx}^2\sigma_{sy}^2\sin^2(2\phi)\right], \tag{11}$$

in which

$$\sigma_{sX}^2(\phi) = (\sigma_{sx}\cos\phi)^2 + (\sigma_{sy}\sin\phi)^2. \tag{12}$$

Here σ_{sX} stands for the rms slope along the ϕ direction. We can see that α_K is related to the fourth-order statistics, for which only *even* powers of γ_X/σ_{sX} are involved in Eq. (9). This means that the associated slope PDF remains symmetric $[p_s(-\gamma_X) = p_s(\gamma_X)]$ because a Gaussian process is symmetric. Conversely, α_S is related to the third-order statistics, for which only *odd* powers of γ_X/σ_{sX} are involved in Eq. (9). This means that the associated slope PDF becomes asymmetric $[p_s(-\gamma_X) \neq p_s(\gamma_X)]$. When $\alpha_K = \alpha_S = 0$, the slope PDF is Gaussian and, as $\sigma_{sX}(0) = \sigma_{sX}(\pi)$, the behavior of the sea is similar in the upwind and downwind directions. For $\{\alpha_S \neq 0,\ \alpha_K = 0\}$, because $\alpha_S(\pi) = -\alpha_S(0)$ [see Eq. (10)], there is an asymmetry between the upwind and downwind directions. For $\{\alpha_S = 0,\ \alpha_K \neq 0\}$, as $\alpha_K(0) = \alpha_K(\pi)$ [Eq. (11)], the slope PDF keeps the same symmetry properties as Gaussian statistics. For all cases we have $\alpha_{S,K}(\pi + \phi) = \alpha_{S,K}(\pi - \phi)$ and $\sigma_{sX}(\pi + \phi) = \sigma_{sX}(\pi - \phi)$, which implies that downwind direction $\phi = \pi$ is a symmetry axis.

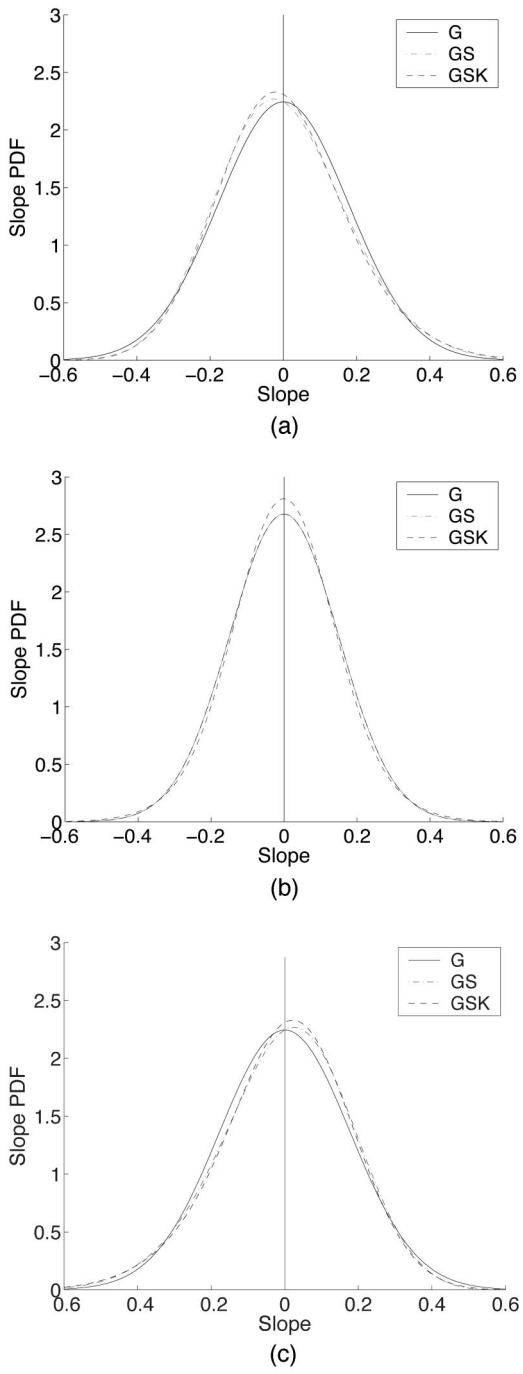

Fig. 4. Marginal slope PDF $p_s(\gamma_X)$ versus slope γ_X. Wind speed, u_{12} = 10 m/s. Wind direction ϕ is equal to 0°, 90°, and 180° in (a), (b), and (c), respectively. G means that the statistics are Gaussian, GS means that the second- and the third-order statistics are included, and GSK means that the second-, third-, and fourth-order statistics are included.

To illustrate the above remarks, in Fig. 4 the marginal slope PDF, $p_s(\gamma_X)$, is plotted versus slope γ_X for wind speed u_{12} = 10 m/s and for wind directions ϕ = {0° [Fig. 4(a)], 90° [Fig. 4(b)], 180° [Fig. 4 (c)]}. In Fig. 4, G means that the statistics are Gaussian, GS means that the second- and the third-order statistics are included, and GSK means that the second-,

third-, and fourth-order statistics are included. S and K refer to the skewness and the kurtosis, respectively, of the sea's surface. In the cross-wind direction, i.e. when $\phi = 90°$, we can see that the skewness effect vanishes because from Eq. (10) we have $\alpha_S = 0$. Thus the slope PDF is symmetric because only even powers of γ_X are involved in Eq. (9). We can also note that the kurtosis effect produces an occurrence of small slopes close to zero weakly greater than a Gaussian slope PDF. In the upwind ($\phi = 0°$) and downwind ($\phi = 180°$) directions, the mean value of the slope PDF is slightly shifted either toward the negative slopes for $\phi = 0°$ [from Eq. (10), $\alpha_S \leq 0$ or toward the positive slope for $\phi = 180°$ (from Eq. (10), $\alpha_S \geq 0$). Thus, as expected, the skewness effect produces an asymmetry of the slope PDF because it is related to the odd powers of γ_X in Eq. (9).

3. Derivation of the Average Shadowing Function

After simple but tedious calculations, the substitution of Eq. (9) into Eqs. (2) yields

$$\Lambda(\upsilon) = \Lambda_G(\upsilon) + \alpha_S\Lambda_S(\upsilon) + \alpha_K\Lambda_K(\upsilon), \tag{13}$$

where

$$\Lambda_G(v) = \frac{\exp(-v^2) - v\sqrt{\pi}\,\mathrm{erfc}(v)}{2v\sqrt{\pi}}, \tag{14a}$$

$$\Lambda_S(v) = -\frac{\exp(-v)^2}{3\sqrt{2\pi}}, \tag{14b}$$

$$\Lambda_K(v) = \frac{(2v^2 - 1)\exp(-v)^2}{6v\sqrt{\pi}}, \tag{14c}$$

in which

$$v(\theta,\ \phi) = \frac{\mu}{\sigma_{sX}\sqrt{2}} = \frac{\cot\theta}{\{2[(\sigma_{sx}\cos\phi)^2 + (\sigma_{sy}\sin\phi)^2]\}^{1/2}}. \tag{15}$$

The function erfc is the complementary error function. Parameter v is proportional to the ratio of the emission ray slope, μ, over the slope's rms defined along the ϕ direction. The shadowing function given by Eq. (5), $S(\theta, \phi|\gamma_X)$, corresponds to the statistical shadowing function averaged over the surface heights. To take the restriction over the surface slopes into account, statistical shadowing function $S(\theta, \phi|\gamma_X)$ is also averaged over the slopes, γ_X giving the average shadowing function $S(\theta, \phi)$. After simple but tedious manipulations, the resultant equation is

$$S(\theta,\ \phi) = \int_{-\infty}^{+\infty} S(\theta,\ \phi\,|\,\gamma_X) \times p_s(\gamma_X)\mathrm{d}\gamma_X = \Omega(\upsilon)/[\Lambda(\upsilon) + 1], \tag{16}$$

in which

$$\Omega(\upsilon) = \Omega_G(\upsilon) + \alpha_S\Omega_S(\upsilon) + \alpha_K\Omega_K(\upsilon), \tag{17}$$

$$\Omega_G(v) = [1 + \mathrm{erf}(v)]/2, \tag{18a}$$

$$\Omega_S(v) = \frac{(2v^2 - 1)\exp(-v^2)}{3\sqrt{2\pi}}, \tag{18b}$$

$$\Omega_K(v) = \frac{v(2v^2 - 3)\exp(-v^2)}{3\sqrt{\pi}}. \tag{18c}$$

In Fig. 5 the average shadowing function $\Omega(v)/[\Lambda(v) + 1]$ is plotted versus emission angle θ for wind speed $u_{12} = 10$ m/s and for wind directions $\phi = \{0°$ [Fig. 5(a)], 90° [Fig. 5(b)], 180° [Fig. 5(c)]$\}$. In the figures G, GS, and GSK mean that $\{\Lambda = \Lambda_G,\ \Omega = \Omega_G\}$, $\{\Lambda = \Lambda_G + \alpha_S\Lambda_S,\ \Omega = \Omega_G + \alpha_S\Omega_S\}$, and $\{\Lambda = \Lambda_G + \alpha_S\Lambda_S + \alpha_K\Lambda_K,\ \Omega = \Omega_G + \alpha_S\Omega_S + \alpha_K\Omega_K\}$, respectively. We can observe that the average shadowing function decreases when the emission angle increases. In fact, as shown in Ref. 23 for Gaussian statistics, the shadowing effect can be ignored for $v \geq 2$, corresponding from Eq. (15) to emission angle $\theta_l(\phi) = \mathrm{arccot}(2\sqrt{2}\sigma_{sX})$, below which the shadowing effect can be ignored. Indeed, for $v = 2$, from Eqs. (13) and (17), $S(\theta, \phi) \approx (0.997 - 0.0035\alpha_K + 0.017\alpha_S)/(1 + 0.006\alpha_K - 0.002\alpha_S) \approx 1$ for small values of $\{\alpha_S, \alpha_K\}$. For instance, with $u_{12} = \{5, 10, 15\}$ m/s and $\phi = 0$, $\sigma_{sX} = \{0.126, 0.178, 0.218\}$ and $\theta_l = \{74°, 63°, 58°\}$, respectively. Figure 5 also shows that the shadowing function varies weakly with ϕ. In the crosswind direction, for which the skewness effect vanishes, the kurtosis does not affect the shadowing, whereas for the upwind and downwind directions the skewness effect slightly affects the shadowing. For instance, with non-Gaussian statistics, for $\theta = 80°$ and $u_{12} = 10$ m/s, the shadowing function is equal to $\{0.760, 0.833, 0.777\}$ for $\phi = \{0°, 90°, 180°\}$, respectively.

3. Emissivity

In this section the emissivity, in which the shadowing function is taken into account, is derived for any surface statistics and applied to the Cox–Munk slope PDF. The emissivity is a number that varies from 0 to 1, which describes the efficiency of thermal radiation of an object.

A number of so-called windows exists in the practical range of the infrared radiation spectrum. In these windows the transmittance of the infrared radiation is high. The windows of practical interest for the infrared optronic systems are 8–13 and 3–5 μm; the near-infrared window of interest is 0.7–2 μm. Between these windows there are absorption bands, which are due mainly to the presence of water vapor and carbon dioxide. In this paper we focus on both infrared windows by choosing wavelengths of 4 and 10 μm.

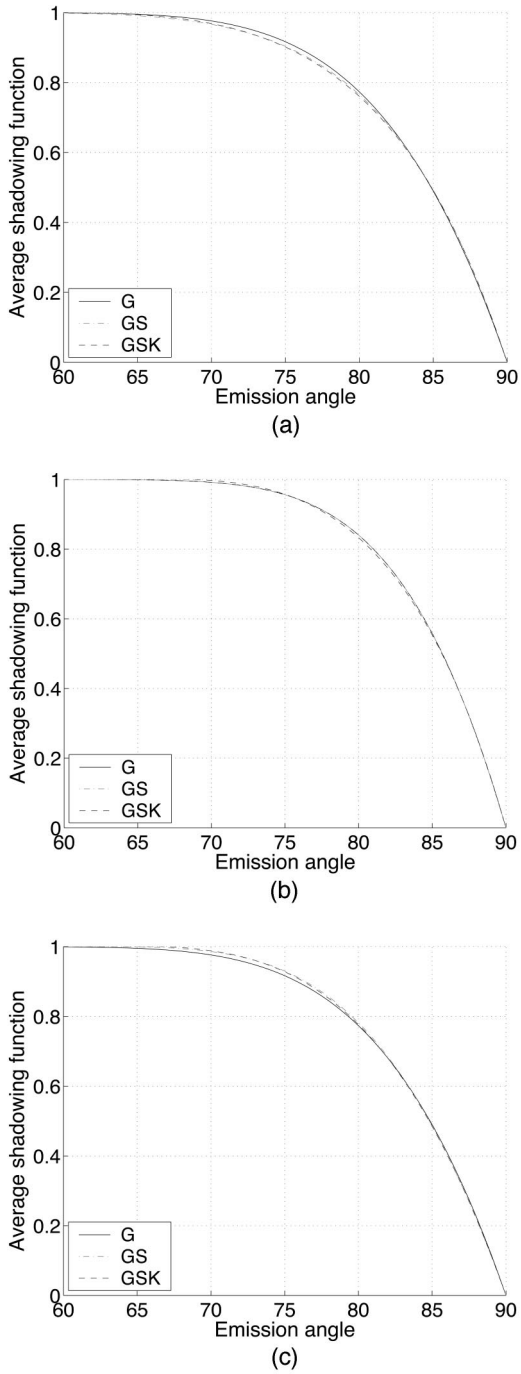

Fig. 5. Average shadowing function $\Omega/(\Lambda + 1)$ versus emission angle θ. Wind speed, $u_{12} = 10$ m/s. Wind direction ϕ is equal to 0°, 90°, and 180° in (a), (b), (c), respectively. G means that the statistics are Gaussian, GS means that the second- and third-order statistics are included, and GSK means that the second-, third-, and fourth-order statistics are included.

A. Derivation of the Emissivity

From the approach developed by Yoshimori *et al.*,[7] Bourlier *et al.*[8,9] showed for a two-dimensional anisotropic rough surface and for any surface slope PDF, $p_s(\gamma_x, \gamma_y)$, that emissivity $\varepsilon(\theta, \phi)$ is given by

$$\varepsilon(\theta,\ \phi) = \int_{-\infty}^{+\infty}\int_{-\infty}^{+\infty} [1 - |r(|\psi|)|^2]\, p_s(\gamma_x,\ \gamma_y) \times g \times S \mathrm{d}\gamma_x \mathrm{d}\gamma_y, \tag{19}$$

where $\{\gamma_x, \gamma_y\}$ are the surface slopes in the upwind ($\phi = 0°$) and crosswind ($\phi = 90°$) directions, respectively. Function g is defined as

$$g(\theta,\ \phi;\ \gamma_x,\ \gamma_y) = 1 - (\gamma_x \cos\phi + \gamma_y \sin\phi)\tan\theta. \tag{20}$$

A physical explanation of g is given by Theiler and Henderson.[30] In Eq. (19), because the electromagnetic radiation is taken to be unpolarized, the reflection coefficient is $r = (r_V + r_H)/2$. r_V is the Fresnel coefficient defined in V polarization (electric vector parallel to the incidence plane), and r_H is the Fresnel coefficient defined in H polarization (electric vector orthogonal to the incidence plane). They are expressed as follows:

$$r_V(\psi) = \frac{n\cos\psi - \cos\psi'}{n\cos\psi + \cos\psi'}, \qquad r_H(\psi) = \frac{\cos\psi - n\cos\psi'}{\cos\psi + n\cos\psi'}, \tag{21}$$

where n is the sea's refractive index (the air's refractive index is assumed to be 1). ψ stands for the local angle with respect to the normal to the facet. It is defined as

$$\cos[\psi(\theta,\ \phi;\ \gamma_x,\ \gamma_y)] = \frac{g \times \cos\theta}{(1 + {\gamma_x}^2 + {\gamma_y}^2)^{1/2}}, \tag{22}$$

and ψ' is the refraction angle that can be found from the Snell–Descartes law, $\sin(\psi') = \sin(\psi)/n$.

Equation (19) shows that one obtains the emissivity by averaging the local emissivity, $1 - |r(|\psi|)|^2$, given by the Kirchhoff law, over the surface slopes. For a stationary process the surface correlation functions (height, slope, curvature, and so on) depend on the difference in horizontal distance between two points on the surface. One obtains the emissivity by calculating the correlation of the scattered field evaluated on a arbitrary point on the surface. Thus the emissivity depends on the correlation. Nevertheless, the geometric optics approximation states that the emissivity does not vanish if the correlation between two adjacent points is strong. This is why the emissivity with single reflection does not depend on the surface correlation and depends on the slope PDF.

The substitution of Eq. (5) into Eq. (19) yields

$$\varepsilon(\theta,\ \phi) = \frac{1}{1 + \Lambda(\theta,\ \phi)} \int_{-\infty}^{\mu} \mathrm{d}\gamma_X \times \int_{-\infty}^{+\infty} [1 - |r(|\psi|)|^2] p_s(\gamma_x,\ \gamma_y)\left(1 - \frac{\gamma_X}{\mu}\right)\mathrm{d}\gamma_Y, \tag{23}$$

where

$$\cos[\psi(\theta;\gamma_X,\ \gamma_Y)] = \frac{1-(\gamma_X/\mu)\cos\theta}{\left(1+\gamma_X^2+\gamma_Y^2\right)^{1/2}}. \qquad (24)$$

The slopes $\{\gamma_x, \gamma_y\}$ are expressed from $\{\gamma_X, \gamma_Y\}$ within Eqs. (4). Inasmuch as the shadowing effect carries a restriction over surface slope γ_X, the upper limit in the integral over γ_X of Eq. (23) is $\mu = \cot\theta$ instead of $+\infty$. The emissivity is positive if $1 - \gamma_X/\mu \geq 0$, which is similar to $\gamma_X \leq \mu$. This condition is fulfilled because of the shadowing function. Using another approach to calculate the shadowing function, Theiler and Henderson[30] arrived at a similar conclusion. In addition, when emission angle θ tends toward 90° (grazing angle), $\tan\theta = 1/\mu$ tends toward infinity and the emissivity diverges owing to the term $1 - \gamma_X/\mu$ in Eq. (23), which has no physical meaning. However, if the shadowing is taken into account, the emissivity converges toward a constant because, from Eqs. (2), we have

$$\lim_{\theta\to\pi/2}\frac{\tan\theta}{1+\Lambda(\theta,\ \phi)} = \left[\int_0^{+\infty}\gamma_X p_s(\gamma_X)\mathrm{d}\gamma_X\right]^{-1}. \qquad (25)$$

For instance, for Gaussian statistics, where

$$p_s(\gamma_x,\ \gamma_y) = \frac{1}{2\pi\sigma_{sx}\sigma_{sy}}\exp\left(-\frac{\gamma_x^2}{2\sigma_{sx}^2}-\frac{\gamma_y^2}{2\sigma_{sy}^2}\right),$$

Eq. (3) becomes $p_s(\gamma_X) = \exp[-\gamma^2/(2\sigma_{sX}^2)]$, where $\sigma_{sX}^2 = (\sigma_{sx}\cos\phi)^2 + (\sigma_{sy}\sin\phi)^2$ is the slope variance along the ϕ direction and $\{\sigma_{sx}, \sigma_{sy}\}$ are the slope rms along the upwind and crosswind directions, respectively. The above limit is then equal to $\sqrt{2\pi}/\sigma_{sX}$. Hence, for grazing emission angles, it is relevant to account for the shadowing effect.

For emission angles close to zero, we have $\mu \to \infty$ and, from Eq. (2), $\Lambda \to 0$. Moreover, assuming that $\gamma_X^2 + \gamma_Y^2 \ll 1$, from Eq. (23) the emissivity becomes

$$\begin{aligned}\varepsilon(0,\ \phi) &\approx [1-|r(0)|^2]\int_{-\infty}^{+\infty}\int_{-\infty}^{+\infty}p_s(\gamma_x,\ \gamma_y)\mathrm{d}\gamma_X\mathrm{d}\gamma_Y \\ &= 1-|r(0)|^2 = 1-\left|\frac{n-1}{n+1}\right|^2. \end{aligned} \qquad (26)$$

We then obtain the emissivity of a plane surface, which is independent of the wind direction.

B. Application to Gaussian and Non-Gaussian Statistics

The emissivity defined in Eq. (23) requires only twofold numerical integrations over the slopes $\{\gamma_X, \gamma_Y\}$. To evaluate this double integral accurately and quickly, we use the method reported in Ref. 8 and summarized in this paper. In Eq. (23), the significant ranges of integration over $\{\gamma_X, \gamma_Y\}$ are determined by the exponential function,

$$\exp\left(-\frac{\gamma_x^2}{2\sigma_{sx}^2}-\frac{\gamma_y^2}{2\sigma_{sy}^2}\right),$$

provided by the slope PDF given by Eq. (6). The slopes $\{\gamma_x, \gamma_y\}$ are replaced by $\{\gamma_X, \gamma_Y\}$ from the variable transformations given by Eqs. (4). The exponential term then becomes $\exp(-a\gamma_Y^2 - 2b\gamma_Y\gamma_X - c\gamma_X^2)$, in which

$$a = \frac{\alpha+\beta\cos(2\phi)}{2(\alpha^2-\beta^2)},$$

$$b = \frac{\beta\sin(2\phi)}{2(\alpha^2-\beta^2)},$$

$$c = \frac{\alpha-\beta\cos(2\phi)}{2(\alpha^2-\beta^2)},$$

where $\alpha = (\sigma_x^2 + \sigma_y^2)/2$ and $\beta = (\sigma_x^2 - \sigma_y^2)/2$. All these quantities are positive because $\sigma_x \geq \sigma_y > 0$. The integration limits over γ_Y are then chosen as $\gamma_Y \in [-4/\sqrt{a}; 4/\sqrt{a}]$ because $\exp(-4^2) = 1.12 \times 10^{-7}$, and over γ_X as $\gamma_X \in [-4/\sqrt{c}; \mu]$. If $\mu > 4/\sqrt{c}$, then the upper limit is $4/\sqrt{c}$. A study of the number of samples N for each integration over $\{\gamma_X, \gamma_Y\}$ showed that the value $N = 80$ is sufficient.

The emissivity depends on the Fresnel coefficients expressed in V and H polarizations [Eq. (21)], for which the sea's refractive index has to be known. It is given by the results provided by Hale and Querry,[31] for which the sea is considered pure water.

1. *Numerical Results versus the Emission Angle*

In Fig. 6 the unpolarized emissivity is plotted versus emission angle θ for wind direction $\phi = 0$ and for wind speed $u_{12} = 10$ m/s. In Fig. 6(a) the wavelength is $\lambda = 4$ μm, whereas in Fig. 6(b) $\lambda = 10$ μm. The abbreviations are similar to those of Figs. 4 and 5. The solid curves, denoted Flat are the emissivities of a flat sea surface.

As the emission angle increases, the emissivity decreases. In Fig. 6, Δ_ε, denotes the emissivity difference, defined as $\Delta_\varepsilon = \varepsilon(0, \phi) - \varepsilon(\pi/2, \phi)$. For example, for Gaussian statistics and for wind speeds $u_{12} = \{5, 10, 15\}$ m/s, we have $\Delta_\varepsilon = \{0.418, 0.316, 0.261\}$ for $\lambda = 4$ μm and $\Delta_\varepsilon = \{0.386, 0.285, 0.231\}$ for $\lambda = 10$ μm. This shows that Δ_ε decreases as the wind speed and the wavelength increase. In addition, one can see that within Δ_ε the kurtosis effect insignificantly affects the emissivity. The skewness effect, however, produces weak diminution of the emissivity for grazing angles, increases for higher wind speeds (according to simulations not reported in this paper for $u_{12} = \{5, 15\}$ m/s, and does not depend on wavelength. For instance, for wind speeds $u_{12} = \{5, 10, 15\}$ m/s, the emissivity difference between Gaussian and non-Gaussian statistics is $\Delta_\varepsilon^{\mathrm{GSK}} - \Delta_\varepsilon^{\mathrm{G}} = \{0.008, 0.018, 0.024\}$ for $\lambda = 4$ μm and $\Delta_\varepsilon^{\mathrm{GSK}} - \Delta_\varepsilon^{\mathrm{G}} = \{0.008, 0.016, 0.022\}$ for $\lambda = 10$ μm.

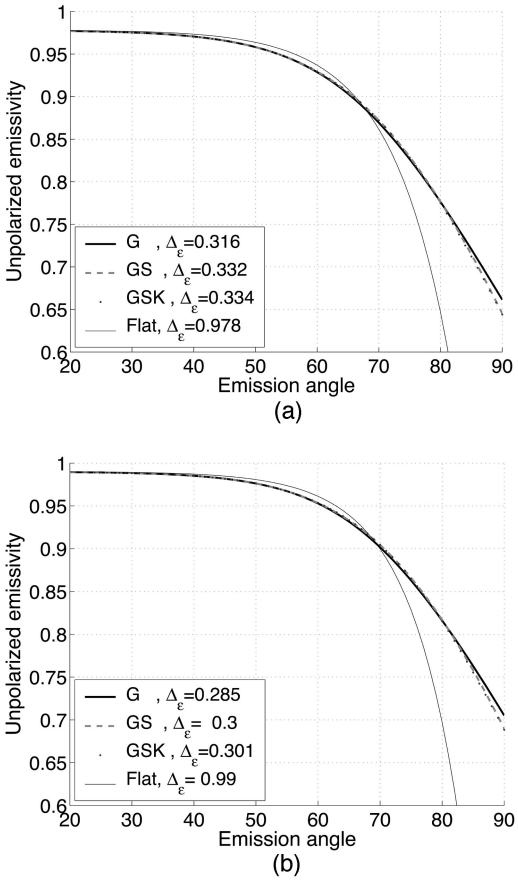

Fig. 6. Unpolarized emissivity versus emission angle θ for wind direction $\phi = 0$ and for wind speed $u_{12} = 10$ m/s. (a) Wavelength $\lambda = 4$ μm; (b) $\lambda = 10$ μm. G means that the statistics are Gaussian, GS means that the second- and the third-order statistics are included, and GSK means that the second-, third-, and fourth-order statistics are included. In addition, Δ_ε denotes the emissivity difference, defined as $\Delta_\varepsilon = \varepsilon(0, \phi) - \varepsilon(\pi/2, \phi)$.

Many infrared sensors measure the SST, T, which is related to $\{T_S, \varepsilon\}$, where T_S is the sea temperature, by writing $L(\lambda, T) = \varepsilon(\theta, \phi; \lambda, u_{12}) \times L(\lambda, T_S)$, where $L(\lambda, T) = C_1\lambda^{-5}/\exp[C_2/(\lambda T) - 1]$ is the Planck distribution (with $C_1 = 1.192 \times 10^{-16}\,\mathrm{W/m^2}$ and $C_2 = 1.439 \times 10^{-2}$ mK). For a blackbody, $\varepsilon = 1$ and $T = T_S$. Thus we can show that

$$\frac{\Delta\varepsilon}{\varepsilon} \approx \frac{d\varepsilon}{\varepsilon} = \Delta T \frac{C_2}{\lambda T^2} \frac{e^x}{e^x - 1},$$

where $x = C_2/(\lambda T)$. For $x \gg 1$ we obtain that $\Delta\varepsilon/\varepsilon \approx \Delta T(C_2/\lambda T^2)$. With $T = 15$ °C, an accuracy in ΔT of 0.1 K (which corresponds approximately to the resolution of infrared cameras) implies accuracies in the relative emissivity $\Delta\varepsilon/\varepsilon$ of 0.42% for a wavelength of 4 μm and of 0.17% for a wavelength of 10 μm.

In Fig. 7, to test the validity of relation (26), which assumes a plane sea surface, limit angle θ_{pl} is plotted versus wind speed u_{12}; θ_{pl} corresponds to the angle below which the relative error of the emissivities between a flat surface and a rough surface is smaller

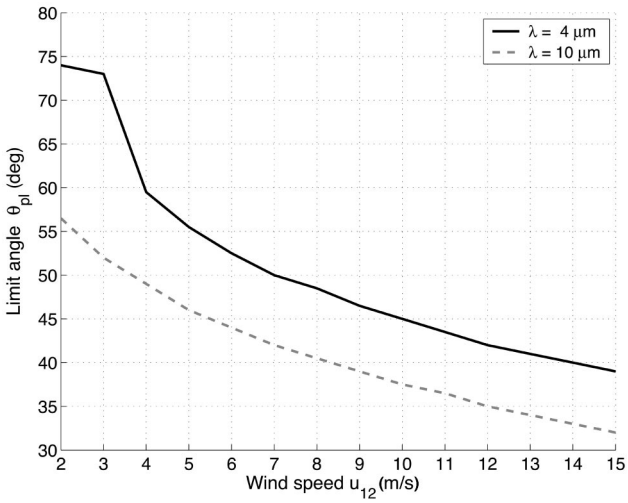

Fig. 7. Limit angle θ_{pl} versus wind speed u_{12}, below which the sea's surface can be considered plane.

than 0.42% and 0.17% for wavelengths of 4 and 10 μm, respectively. As the surface roughness (or the wind speed) and the wavelength increase, the limit angle decreases. For emission angles smaller than θ_{pl}, the emissivity does not depend on the surface roughness, and it is given by a flat surface. For instance, with λ equal to 4 or 10 μm, the sea's refractive index is $n = \{1.351 + 0.005j, 1.218 + 0.051j\}$,[31] and $\varepsilon(0, \phi) = \{0.978, 0.990\}$ for $\theta \le \theta_{pl}$.

2. *Numerical Results versus Wind Direction*

In Fig. 8 the unpolarized emissivity is plotted versus wind direction φ for emission angle $\theta = 80°$, for wind speed $u_{12} = 5$ m/s, and wavelengths 4 and 10 μm. In Fig. 9 the same variation as in Fig. 8 is plotted for a wind speed $u_{12} = 15$ m/s. The abbreviations are similar to those of Figs. 4 and 5.

For any statistics, Figs. 8 and 9 reveal that the emissivity is symmetric along the downwind direction, i.e., $\varepsilon(\theta, \pi + \phi) = \varepsilon(\theta, \pi - \phi)$. This symmetry can be explained as follows: The emissivity computed from Eq. (23) depends on slope γ_Y because the angle $\psi(\theta; \gamma_X, \gamma_Y)$ and slope PDF [in which the slopes (γ_X, γ_Y) are expressed from Eqs. (4)], $p_s(\gamma_X, \gamma_Y)$, depend on γ_Y. Inasmuch as slope γ_Y is much smaller than unity, we can approximate ψ as $\cos(\psi) \approx (1 - \gamma_X/\mu)\cos\theta/(1 + \gamma_X^2)^{1/2}$, which is independent of γ_Y. Thus we can integrate slope PDF $p_s(\gamma_X, \gamma_Y)$ over γ_Y, obtaining the marginal PDF, $p_s(\gamma_X)$, expressed from Eq. (9). The resultant expression of the emissivity is then

$$\varepsilon(\theta, \phi) \approx \frac{1}{1 + \Lambda(\theta, \phi)} \int_{-\infty}^{\mu} [1 - |r(|\psi|)|^2] \times p_s(\gamma_X)\left(1 - \frac{\gamma_X}{\mu}\right) d\gamma_X. \quad (27)$$

In addition, as slope $p_s(\gamma_X)$ is symmetric with respect to the downwind direction, the emissivity has the

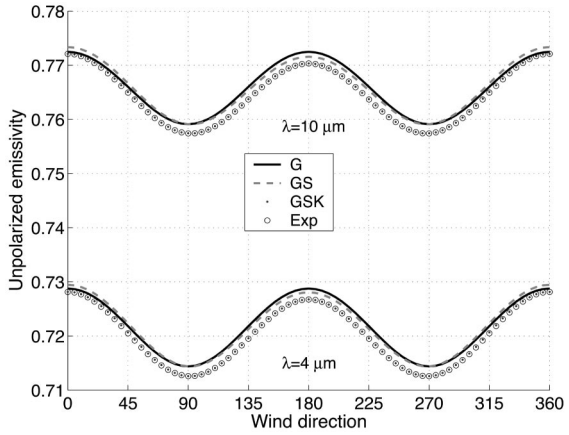

Fig. 8. Unpolarized emissivity versus wind direction ϕ for emission angle $\theta = 80°$ for wind speed $u_{12} = 5$ m/s and for wavelengths 4 and 10 μm. G means that the statistics are Gaussian, GS means that the second- and the third-order statistics are included, and GSK means that the second-, third-, and fourth-order statistics are included. In addition, Exp represents the expansion of the emissivity as a cosine series $[\cos(n\phi)]$ truncated up to the second order.

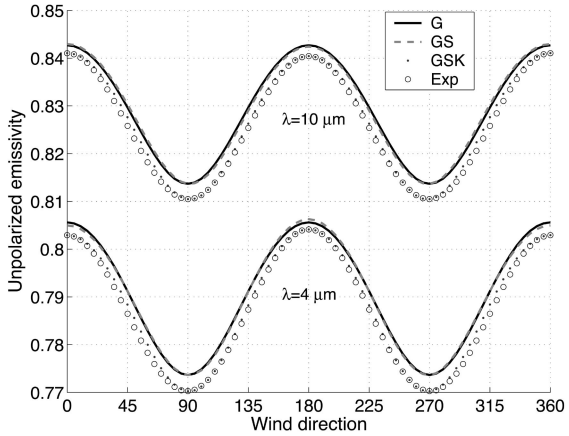

Fig. 9. Same variation as in Fig. 8 for wind speed $u_{12} = 15$ m/s.

same property. The computation of the emissivity requires then only one numerical integration.

For $\phi \in [0; \pi]$ degrees, Figs. 8 and 9 show that, when the wind speed increases, the emissivity becomes more dependent on the wind direction, i.e., on the sea-surface anisotropy. For Gaussian statistics, the emissivity varies as a cosine function with a nonzero mean value [i.e., $\varepsilon(\theta, \phi) \approx \varepsilon_0(\theta) + \varepsilon_2(\theta)\cos(2\phi)$], where its minimum occurs in the cross-wind direction ($\phi = 90°$ and the slope's rms $\sigma_{sX} = \sigma_{sy}$ is minimum]. Conversely, its maximum occurs in the upwind ($\phi = 0°$) and downwind ($\phi = 180°$) directions, for which $\sigma_{sX} = \sigma_{sx}$ is maximum. In addition, one can see that $\varepsilon(\theta, 0) = \varepsilon(\theta, \pi)$ and $\varepsilon(\theta, \pi/2) = \varepsilon(\theta, 3\pi/2)$ because, for a Gaussian process, the slope is symmetric. When the higher-order statistics are taken into account, the emissivity is more sensitive to wind direction for high wind speeds ($u_{12} = 15$ m/s). The emissivity can be modeled with respect to wind direction ϕ as

$$\varepsilon(\theta,\ \phi) \approx \varepsilon_0(\theta) + \varepsilon_1(\theta)\cos(\phi) + \varepsilon_2(\theta)\cos(2\phi), \quad (28)$$

where $\{\varepsilon_{0,1,2}(\theta)\}$ can be found from the values of $\varepsilon(\theta, 0)$, $\varepsilon(\theta, \pi/2)$ and $\varepsilon(\theta, \pi)$ as

$$\begin{aligned} \varepsilon_0(\theta) &= [\varepsilon(\theta,\ 0) + \varepsilon(\theta,\ \pi) + 2\varepsilon(\theta,\ \pi/2)]/4, \\ \varepsilon_1(\theta) &= [\varepsilon(\theta,\ 0) - \varepsilon(\theta,\ \pi)]/2, \\ \varepsilon_2(\theta) &= [\varepsilon(\theta,\ 0) + \varepsilon(\theta,\ \pi) - 2\varepsilon(\theta,\ \pi/2)]/4. \end{aligned} \quad (29)$$

The values $\{\varepsilon_{0,1,2}(\theta)\}$ are given in Table 1 for wavelengths of 4 and 10 μm, for wind speeds of 5 and 15 m/s, and for emission angles of 80° and 85°. $\varepsilon_0(\theta)$ corresponds to the emissivity of an isotropic surface, $\varepsilon_1(\theta)$ corresponds to the asymmetry between the upwind and the downwind directions [for Gaussian statistics, it vanishes because $\varepsilon(\theta, 0) = \varepsilon(\theta, \pi)$] and $\varepsilon_2(\theta)$ corresponds to the asymmetry between the upwind and the crosswind directions. The expansion given by relation (28) is plotted in Figs. 9 and 10 by the circled dots labeled Exp. For non-Gaussian statistics, one can see good agreement between the emissivity and its expansion.

Like Gaussian statistics, the emissivity for non-Gaussian statistics reaches its maximum in the downwind direction ($\phi = 180°$), whereas for the upwind direction ($\phi = 0$) the emissivity is smaller than that obtained with Gaussian statistics. We can show from relation (28) that the minimum of $\varepsilon(\theta, \phi)$ according to $\phi \in [0; \pi]$ is given by $\phi_{\min} \approx \pi/2 + \varepsilon_1(\theta)/[4\varepsilon_2(\theta)]$. $\phi_{\min}$ is given in Table 1 for non-Gaussian statistics. For Gaussian statistics, $\phi_{\min} = 90°$ for any wind speed, any wavelength, and any emission angle.

In Fig. 10, $\Delta_\varepsilon(\theta)$ is plotted versus emission angle for wind speeds $u_{12} = \{5, 15\}$ m/s and wavelengths of 4 and 10 μm. Δ_ε is defined as

$$\Delta_\varepsilon(\theta) = \max_{\phi\in[0;\pi]} \varepsilon(\theta,\ \phi) - \min_{\phi\in[0;\pi]} \varepsilon(\theta,\ \phi).$$

Figure 10 shows that the sea-surface anisotropy effect increases with wind speed and varies insignifi-

Table 1. Coefficients $\{\varepsilon_{0,1,2}(\theta)\}$ of the Emissivity Expansion[a] and the Angle $\phi_{\min}$[b] (deg), Giving the Minimum of $\varepsilon(\theta, \phi)$ for $\phi \in [0; \pi]$ and for a Given θ

θ (°), u_{12} (m/s), λ (μm)	$\varepsilon_0(\theta)$	$\varepsilon_1(\theta)$	$\varepsilon_2(\theta)$	$\phi_{\min}$
80, 5, 4	0.72001	0.00070	0.00743	91.3
80, 5, 10	0.76432	0.00089	0.00690	91.8
80, 15, 4	0.78690	−0.00061	0.01664	89.5
80, 15, 10	0.82560	0.00030	0.01513	90.3
85, 5, 4	0.62913	−0.00220	0.01335	87.6
85, 5, 10	0.67436	−0.00192	0.01318	87.9
85, 15, 4	0.73722	−0.00922	0.02353	84.4
85, 15, 10	0.77831	−0.00769	0.02221	85.0

[a]Defined as $\varepsilon(\theta,\ \phi) = \varepsilon_0(\theta) + \varepsilon_1(\theta)\cos(\phi) + \varepsilon_2(\theta)\cos(2\phi)$.
[b]$\phi_{\min} \approx \pi/2 + \varepsilon_1(\theta)/[4\varepsilon_2(\theta)]$.

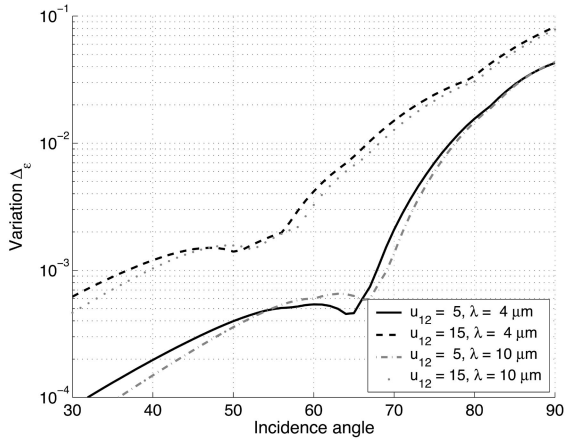

Fig. 10. $\Delta_\varepsilon(\theta)$ plotted versus emission angle θ for non-Gaussian statistics and for wind speeds $u_{12} = \{5, 15\}$ m/s and wavelengths 4 and 10 μm. $\Delta_\varepsilon(\theta) = \max_{\phi\in[0;\pi]}\varepsilon(\theta, \phi) - \min_{\phi\in[0;\pi]}\varepsilon(\theta, \phi)$.

cantly with wave length. For the $\Delta_\varepsilon(\theta) \leq 0.001$, the emissivity does not depend on wind direction ϕ for emission angles θ smaller than {38°, 68°} and for wind speeds $u_{12} = \{5, 15\}$ m/s, respectively. The model of Masuda *et al.*,[4] which assumed an isotropic surface, can then be used if the shadowing effect is also negligible.

3. *Study of the Shadowing and the Statistics*

To study the effects of the shadowing and the statistics in more detail, we define two limit angles, θ_{sh} and θ_{st}. θ_{sh} corresponds to the angle below which the relative errors of the emissivities with non-Gaussian statistics between unshadow and shadow are smaller than 0.42% and 0.17% for 4 and 10 μm wavelengths, respectively. In the same way, θ_{st} corresponds to the angle below which the relative errors of the emissivities with shadow between Gaussian and non-Gaussian statistics do not exceed 0.42% and 0.17% for 4 and 10 μm wavelengths.

In Fig. 11 the limit emission angle, θ_{sh}, is plotted versus wind speed u_{12} and wind direction ϕ for wavelengths equal to 4 and 10 μm. As the wind speed and the wave length increase, θ_{sh} decreases because the shadowing effect increases with the surface roughness, and the criterion of the relative emissivity decreases. The difference in θ_{sh} between $\phi = 0°$ and $\phi = 180°$ increases with wind speed and does not exceed 5°.

In Fig. 12 the limit emission angle, θ_{st} is plotted versus wind speed u_{12} and wind direction for wavelengths equal to 4 and 10 μm. One can observe that θ_{st} decreases as the the wind speed increases, is more sensitive to the wavelength than θ_{sh}, and is smaller than θ_{sh} for high wind speeds. In addition, for $\phi = 90°$, θ_{sh} varies weakly with the wind speed.

4. *Comparison of the Model with a Monte Carlo Ray-Tracing Method*

In this subsection the model is compared with numerical results provided by Henderson *et al.*[19] computed from a Monte Carlo ray-tracing method, where

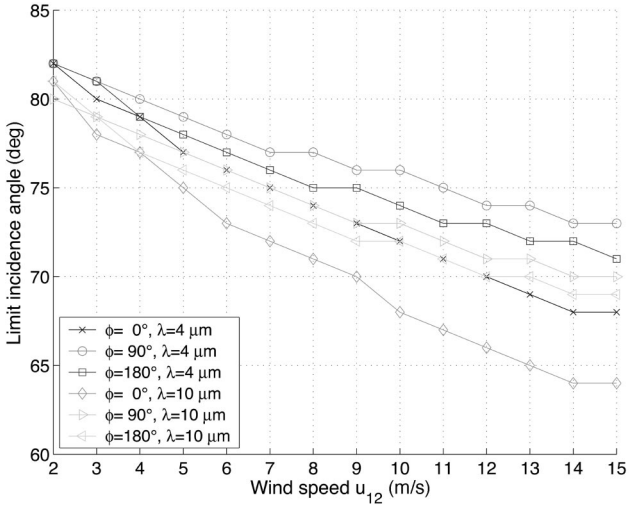

Fig. 11. Limit emission angle, θ_{sh}, below which the shadowing effect can be ignored for non-Gaussian statistics, versus wind speed u_{12}, for wind directions $\phi = \{0°, 90°, 180°\}$ and for wavelengths 4 and 10 μm.

Gaussian statistics of the surface are assumed. Wind direction $\phi = 0$, and wavelength $\lambda = 4$ μm. The emission angle ranges from 0° to 85° in steps of 5°.

In Figs. 13(a) and 13(c), the unpolarized emissivity ε^G (superscript G means for Gaussian statistics) is compared with the numerical results of Henderson *et al.*,[19] referred to in the figure as $\varepsilon^{\mathrm{Num1}}$ and $\varepsilon^{\mathrm{Num2}}$. $\varepsilon^{\mathrm{Num1}}$ neglects the multiple reflections, whereas in the computation of $\varepsilon^{\mathrm{Num2}}$ the multiple reflections are taken into account. The wind speeds are $u_{12} = \{5, 15\}$ m/s in Figs. 13(a), 13(b) in Figs. 13(c), 13(d), respectively. In Figs. 13(b) and 13(d), the emissivity differences $\{|\varepsilon^{\mathrm{Num1}} - \varepsilon^G|, |\varepsilon^{\mathrm{Num2}} - \varepsilon^G|\}$ are plotted versus emission angle. Very good agreement between ε^G and $\varepsilon^{\mathrm{Num1}}$ can be observed which means that the modeling of the shadowing function in the derivation of ε^G is correct. As the emission angle increases, multiple reflections increase, but they decrease from 85° to 90°. The

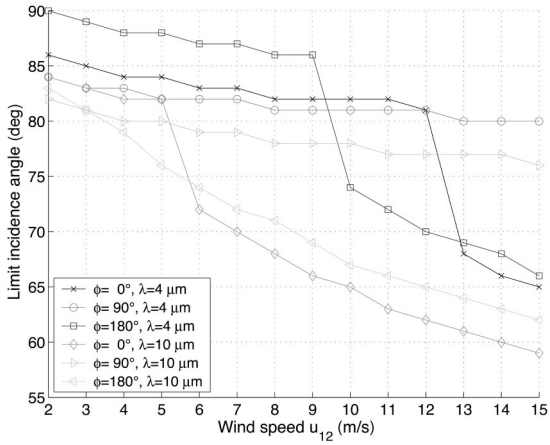

Fig. 12. Limit emission angle below which Gaussian statistics can be considered, θ_{st}, versus wind speed u_{12}, for wind directions $\phi = \{0°, 90°, 180°\}$ and for wavelengths 4 and 10 μm.

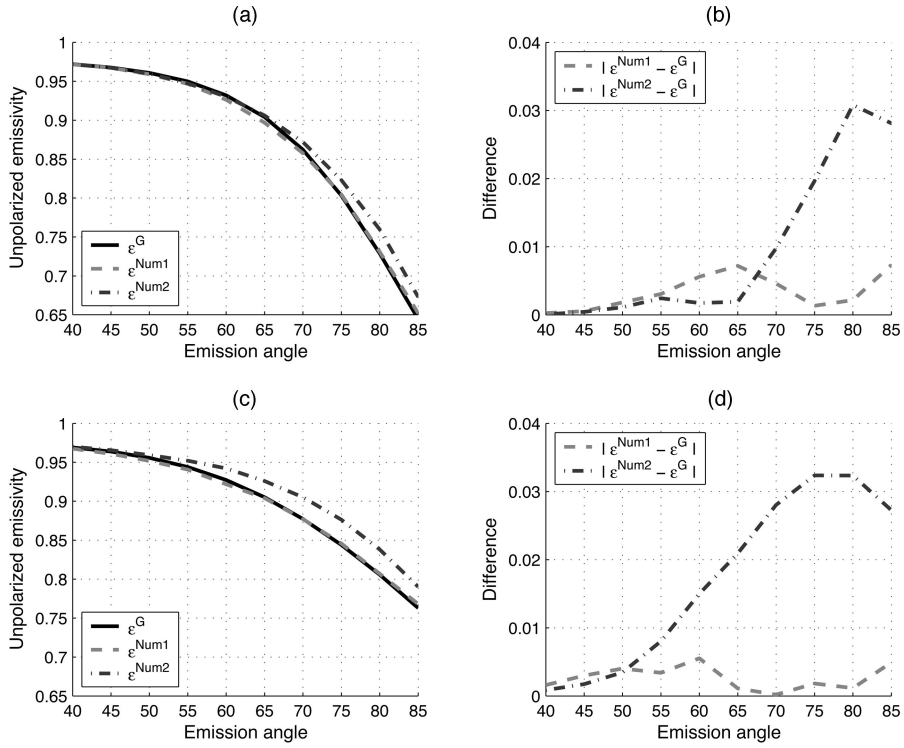

Fig. 13. (a), (c) Comparison of the averaged unpolarized emissivity, ε^G (superscript *G,* for Gaussian statistics), with numerical results $\{\varepsilon^{Num1}, \varepsilon^{Num2}\}$ obtained from a Monte Carlo ray-tracing method[19] versus the emission angle for wind direction $\phi = 0$, wavelength $\lambda = 4$ μm, and $u_{12} = 5$ m/s. ε^{Num1} neglects the multiple reflections, whereas for the computation of ε^{Num2} the multiple reflections are taken into account. The wind speeds are $u_{12} = \{5, 15\}$ m/s for (a), (b) and (c), (d), respectively. (b), (d) Emissivity differences $\{|\varepsilon^{Num1} - \varepsilon^G| \; |\varepsilon^{Num2} - \varepsilon^G|\}$ versus emission angle.

maximum of $|\varepsilon^{Num2} - \varepsilon^G|$ is 0.03 for an emission angle equal to 80°.

5. Comparison with Measurements

In this subsection the emissivity derived from non-Gaussian statistics is compared with experimental data.[17,18] A complete description of the spectral radiance measurements and the technique used for deriving the spectral distribution of ocean emissivity was provided by Niclòs *et al.*[17] and Smith *et al.*[18] In Ref. 17, the emissivity experimental values were determined from thermal infrared radiometric measurements carried out from an oil rig under open Mediterranean sea conditions during the Wind and Salinity Experiment 2000 campaign (WISE 2000) funded by the European Space Agency. The methodology consists of quasi-simultaneous measurements of the radiance coming from the sea's surface and the downwelling sky radiance, in addition to the corresponding sea temperature as a reference. Radiometric data were taken by a CE 312 radiometer, with four channels placed at 8–14 μm intervals. The wind speeds were $u_{12} = \{4.5 \pm 0.9, \; 10.3 \pm 1.1\}$ m/s, and the wind direction was $\phi = 284 \pm 32$. The emission angle θ ranged from 25° to 65° with sampling steps of 10°.

In Fig. 14 our emissivity model is compared with measurements[17] versus the emission angle. In Figs. 14(a)–14(c) the wind speed is $u_{12} = 4.5$ m/s, whereas in Figs. 14(d)–14(f) $u_{12} = 10.3$ m/s. In Figs. 14(a) and 14(d) the unpolarized emissivity is averaged over the range 8.2–9.2 μm; in Figs. 14(b) and 14(c), over 10.5–11.5 μm, and in Figs. 14(c) and 14(f), over 11.5–12.5 μm. The wind direction is $\phi = 284°$. The vertical lines around the curves indicate the error bars. The numerical results are averaged over the wavelength with sampling steps of 0.2 μm, which is sufficient because the sea's refractive index varies weakly with wavelength. In addition, for each point on the curve the error bar is displayed. Its minimum value is obtained for $u_{12} = \{3.6, 9.2\}$ m/s and $\phi = 252°$, whereas its maximum value is obtained for $u_{12} = \{5.4, 11.4\}$ m/s and $\phi = 316°$. For windows 8.2–9.2 μm and 10.5–11.5 μm, there is good agreement between the model and the measurements. Nevertheless, for window 11.5–12.5 μm and for wind speed $u_{12} = 4.5$ m/s [Fig. 14(c)], the curve of the model goes below the data curve. Possible causes are as follows:

- From Fig. 13, this disagreement is not due to the multiple reflections and seems to be independent of the emission angle and the wind speed, because good agreement is found in Fig. 14(f). Niclòs *et al.*[17] reported the same remark by comparing their measurements with the model of Masuda *et al.*,[4] which neglected the shadowing and considered Gaussian statistics.

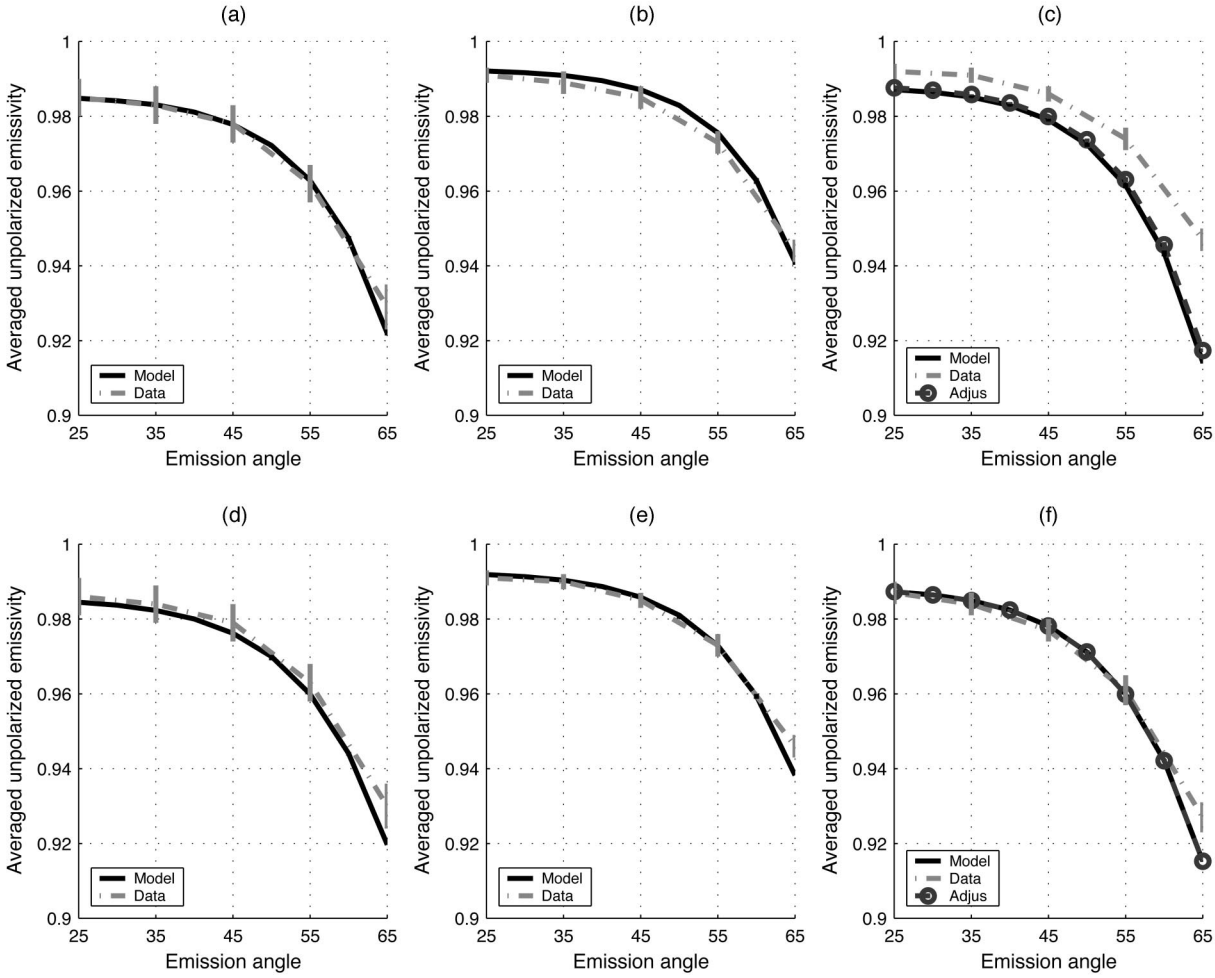

Fig. 14. Comparison of averaged unpolarized emissivity with measurements[17] versus emission angle. (a)–(c) Wind speed, u_{12} = 4.5 m/s; (d)–(f) u_{12} = 10.3 m/s. The unpolarized emissivity is averaged over the ranges (a), (d) 8.2–9.2 μm; (b), (e) 10.5–11.5 μm; and (c), (f) 11.5–12.5 μm. The wind direction is $\phi = 284°$. In addition, in (c) and (f), for the curve denoted Adjus the sea's refractive index is calculated from the adjustment of Friedman.[32]

- It should be noted that the Mediterranean sea is salt water, with a mean value of the salinity equal to 37.8 ± 0.3 practical salinity units. The value of the refractive index that we used for the emissivity computation assumes pure water. Wu[15] and Smith *et al.*[18] studied this aspect in details by using other models of the refractive index, such as the adjustment of Friedman,[32] to introduce the salinity, and that reported in Refs. 33–35. In Figs. 14(c)–14(f), the emissivity is plotted in circled curves denoted Adjus, for which the sea's refractive index is calculated from the adjustment of Friedman.[32] One can observe that the emissivity varies insignificantly.
- The Cox–Slope PDF is valid for near-neutral stability (equal air and water temperatures). Shaw and Churnside[16] showed that the slope's rms can change significantly according to this parameter. Further simulations, not reported in this paper, showed better agreement by varying the wind speed of ±3 m/s (the initial wind speeds were 4.5 and 10.3 m/s). Nevertheless, the numerical results remained below the data.

Thus we can attribute this difference to error in measurements.

In the research reported in Ref. 18 the emissivity was measured on 16 January 1995 in the Gulf of Mexico with a Fourier-transform spectrometer. On the day of the measurement the sky was clear and the wind was calm at approximately 5 m/s for the entire day. The instrument was mounted aboard an oceanographic research vessel, the R. V. Pelican, operated by the Louisiana University Marine Consortium. Spectral radiance was measured, with a spectral resolution of 0.5 cm^{-1}, at emission angles 36.5°, 56.5°, 73.5°. In Fig. 15 the unpolarized emissivity spectrum is compared with measurements[18] of wave number $1/\lambda$ in inverse centimeters. The corresponding range of wavelength λ is 8.55–12.05 μm. The wind speed is u_{12} = 5 m/s, and the wind direction is $\phi = 0$. Inasmuch as the wind direction is not given by Smith *et al.*[18] (an isotropic sea surface is assumed), for each point of the curve an error bar obtained for wind directions $\phi = \{0°, 180°\}$ is displayed. For an emission

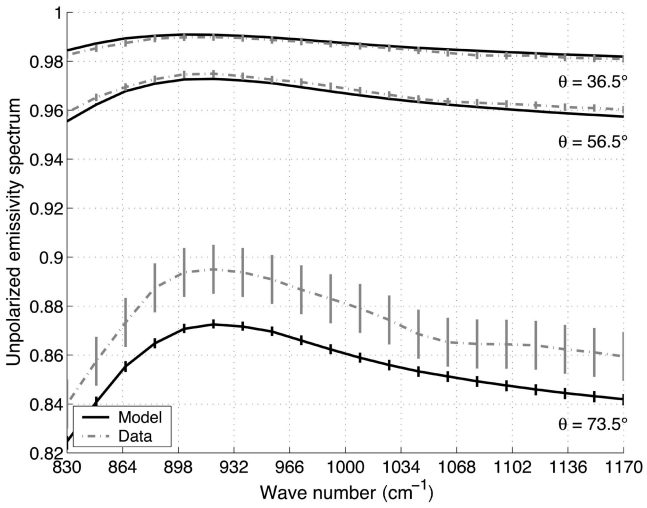

Fig. 15. Comparison of the unpolarized emissivity spectrum with measurements[18] of wave number 1 in inverse centimeters. The wind speed is $u_{12} = 5$ m/s, and the wind direction is $\phi = 0°$.

angle $\theta = 73.5°$ a deviation is noted between the data and the model. Some possible causes of this difference are as follows:

- As shown in Fig. 13 for $u_{12} = 5$ m/s, inclusion of multiple reflections implies an augmentation of the emissivity of 0.02. This result is consistent with the conclusion of the Preisendorfer model,[36] in which the downward albedo is computed with the same procedure as used by Henderson *et al.*[19] Thus the fact that the model underestimates the emissivity seems to be related to the presence of multiple reflections, which are not accounted for in our model.
- For wavelengths of 8.55–12.05 μm, the adjustment that Friedman[32] used for calculation of refractive index of salt water does not affect the emissivity.
- Increasing the wind speed to 3 m/s produces better agreement.
- The measured data shown in Fig. 15 are from a Fourier-transform spectrometer, which has a small but potentially significant polarization sensitivity that can cause a weak overestimation of the emissivity.

Thus we attribute the main cause of the deviation between the data and the model to multiple reflections.

4. Conclusions

In this paper, from a geometric optics approximation of first-order (no multiple reflection), sea-surface emissivity with shadow was derived; the Cox–Munk non-Gaussian slope PDF, in which the third- (related to the skewness) and the fourth- (related to the kurtosis) order statistics are taken into account, was considered. The emissivity was then compared with that obtained from Gaussian statistics, for which the Cox–Munk slope PDF is truncated up to second order, depending then only on the slope's rms. In addition, it was shown that it is relevant to take the shadowing effect into account for grazing emission angles, because the emissivity does not diverge. The emissivity was computed in the 4 and 10 μm atmospheric transmission regions for moderate wind speeds for emission angles ranging from 0° (nadir) to 90° (horizon) and for wind directions ranging from 0° to 360°. Numerical results were also compared with measurements and a Monte Carlo ray-tracing method.

The numerical results show that the emissivity is a decreasing function of the emission angle and increases with wind speed. Comparisons with measurements show good agreement for moderate emission angles, for which the multiple reflections and the shadowing effect can be omitted. Nevertheless, for an emission angle of 73.5°, the comparison with measurements shows that our model underpredicts the data. The comparison with a Monte Carlo ray-tracing method, in which the multiple reflections are taken into account, demonstrates that this disagreement is due to the multiple reflections, which produce an augmentation of the emissivity of 0.03 (Fig. 13). When multiple reflections are ignored in the Monte Carlo simulations, however, they appear to give results in agreement with those computed by our model. Thus the shadowing function that we used in the emissivity computation correctly predicts the shadowing phenomenon.

The higher-order statistics become significant for emission angles larger than 60°, increase with wind speed, and produce a diminution of the emissivity. For any statistics, the numerical results show that the downwind direction is a symmetry axis because the surface slopes are much smaller than unity. The emissivity, Eq. (23), can be approximated by Eq. (27), in which only one numerical integration over the slopes is needed, instead of two, when no assumption is used [see Eq. (23)].

In addition, we have shown that the emissivity can be modeled along wind direction ϕ as an even Fourier series truncated up to second order, $\varepsilon(\theta, \phi) = \sum_{n=0}^{n=2} \varepsilon_n(\theta)\cos(n\phi)$. $\varepsilon_0(\theta)$ is the emissivity of an isotropic surface, $\varepsilon_1(\theta)$ is related to the asymmetry along the upwind and downwind directions (it vanishes for Gaussian statistics), and $\varepsilon_2(\theta)$ is related to the asymmetry along the upwind and crosswind directions. They can be computed from the emissivities evaluated in the upwind, crosswind, and downwind directions. For a given threshold of the emissivity variation along ϕ, Fig. 10 allows one to predict the emission angles below which the sea surface can be considered isotropic.

Figures 11 and 12 give two limit emission angles $\{\theta_{sh}, \theta_{st}\}$ below which the shadowing effect can be ignored and the surface statistics can be assumed Gaussian, respectively. For wind speeds ranging from 2 to 15 m/s, θ_{sh} ranges from 82° to 65°, and these limits vary weakly in ±5° increments with respect to the wind direction. As was shown by Bourlier *et al.*[23] for Gaussian statistics, the shadowing effect can be ignored for emission angles smaller than arccot

$[2\sqrt{2}\sigma_{sX}(\phi)]$, where $\sigma_{sX}(\phi)$ is the slope's rms along ϕ. Using a similar formula for modeling the numerical results of Fig. 11, we find that $\theta_{sh} = \text{arccot}\,[\beta\sqrt{2}\sigma_{sX}(\phi)] \pm 2°$, where $\beta = \{1.2, 1.4\}$ for wavelengths $\lambda = \{4, 10\}$ μm. For wind speeds ranging from 2 to 15 m/s, θ_{st} ranges from 60° to 90° and is more sensitive to the wind direction than is θ_{sh}. This study also presents a criterion, plotted in Fig. 7, that gives a limit emission angle below which the sea's surface can be considered plane.

For emission angles close to the horizon, it was demonstrated in this paper that the emissivity calculation has to account for the multiple reflections and the shadowing effect, and the surface statistics have to be considered non-Gaussian. The first and second effects were studied by Henderson *et al.*[19] and Preisendorfer[36] from a Monte Carlo method. Such a method needs a long computing time, because one needs to consider a large number of rays and surface realizations to reproduce the surface statistics and to average the emissivity. To our knowledge, the last-named effect has not been investigated with a Monte Carlo method. One objective of this paper would be to derive the contribution of the second-order reflection to the emissivity by including the shadowing effect also. A derivation of the shadowing function with multiple reflections has been made by Bourlier *et al.*[37]

For calculating the radiance received by a sensor (see, for instance, Zeiss *et al.*[10] and Shaw[11]), other parameters must be known, such as the radiance emitted by the atmosphere between the sensor and the surface, the radiance emitted by the atmosphere (sky, Sun, cloud, . . .) and reflected by the surface, and the atmospheric transmission coefficient along the sea-surface sensor path. The atmospheric transmission coefficient and the atmospheric radiance can be computed from a MODTRAN program.[38] The sea-surface reflectivity, related to the surface slope PDF, can be obtained from the model of Bourlier *et al.*,[9] in which multiple reflections are ignored and shadowing with Gaussian statistics is considered. For non-Gaussian statistics the slope PDF and the parameter Λ [related to the shadowing function and given by Eq. (13)] must then be substituted by those used for Gaussian statistics.

The author thanks Bradley G. Henderson for providing his numerical results and Raquel Niclòs for helpful discussions with regard to his measurements. I thank my colleagues, N. De Beaucoudrey, N. Déchamps, and N. Pinel, for their useful comments. I also thank the anonymous reviewers whose relevant comments influenced the final appearance of this paper.

References

1. X. Wu and W. L. Smith, "Emissivity of rough sea surface for 8–13 μm: modeling and verification," Appl. Opt. **36,** 2609–2619 (1997).
2. J. A. Shaw and C. Marston, "Polarized infrared emissivity for a rough water surface," Opt. Express **7,** 375–380 (2000).
3. P. D. Watts, M. R. Allen, and T. J. Nightingale, "Wind speed effects on sea surface emission and reflection for the along track scanning radiometer," J. Atmos. Ocean. Technol. **13,** 126–141 (1996).
4. K. Masuda, T. Takashima, and Y. Takayama, "Emissivity of pure and sea waters for the model sea surface in the infrared window regions," Remote Sens. Environ. **24,** 313–329 (1988).
5. P. M. Saunders, "Shadowing on the ocean and the existence of the horizon," J. Geophys. Res. **72,** 4643–4649 (1967).
6. K. Yoshimori, K. Itoh, and Y. Ichioka, "Thermal radiative and reflective characteristics of a wind-roughened water surface," J. Opt. Soc. Am. **11,** 1886–1893 (1994).
7. K. Yoshimori, K. Itoh, and Y. Ichioka, "Optical characteristics of a wind-roughened water surface: a two-dimensional theory," Appl. Opt. **34,** 6236–6247 (1995).
8. C. Bourlier, J. Saillard, and G. Berginc, "Effect of the observation length on the two-dimensional shadowing function of the sea surface: application on infrared 3–13 μm emissivity," Appl. Opt. **39,** 3433–3442 (2000).
9. C. Bourlier, G. Berginc, and J. Saillard, "Theoretical study on two-dimensional Gaussian rough sea surface emission and reflection in the infrared frequencies with shadowing effect," IEEE Trans. Geosci. Remote Sens. **39,** 379–392 (2001).
10. C. R. Zeiss, C. P. MacGrath, K. M. Littfin, and H. G. Hughes, "Infrared radiance of the wind-ruffled sea," J. Opt. Soc. Am. A **16,** 1439–1452 (1999).
11. J. A. Shaw, "Polarimetric measurements of long-wave infrared spectral radiance from water," Appl. Opt. **38,** 379–392 (1999).
12. D. E. Freund, R. J. Joseph, D. J. Donohue, and K. T. Constantikes, "Numerical computations of rough sea surface emissivity using the interaction probability," J. Opt. Soc. Am. A **14,** 1836–1849 (1997).
13. C. Cox and W. Munk, "Measurement of the roughness of the sea surface from photographs of the sun's glitter," J. Opt. Soc. Am. **44,** 838–850 (1954).
14. P. A. Hwang and O. H. Shemdin, "The dependence of sea surface slope on atmospheric stability and swell conditions," J. Geophys. Res. **93**(C11), 13,903–13,912 (1988).
15. J. Wu, "Effects of atmospheric stability on ocean ripples: a comparison between optical and microwave measurements," J. Geophys. Res. **96**(C4), 7265–7269 (1991).
16. J. A. Shaw and J. H. Churnside, "Scanning-laser glint measurements of sea-surface slope statistics," Appl. Opt. **36,** 4202–4213 (1997).
17. R. Niclòs, E. Valor, V. Caselles, and C. Coll, "Sea surface emissivity angular measurements. Comparison with theoretical models," in *Remote Sensing of the Ocean and Sea Ice 2003*, C. R. Bostates Jr., and R. Santolen eds., SPIE **5233,** 348–356 (2003).
18. W. L. Smith, R. O. Knuteson, H. E. Revercomb, W. Feltz, H. B. Howell, W. P. Menzel, N. R. Nalli, O. Brown, J. Brown, P. Minnett, and W. McKeown, "Observations of the infrared radiative properties of the ocean-implications for the measurement of sea surface temperature via satellite remote sensing," Bull. Am. Meteorol. Soc. **77,** 41–51 (1996).
19. B. G. Henderson, J. Theiler, and P. Villeneuve, "The polarized emissivity of a wind-roughened sea surface: a Monte Carlo model," Remote Sens. Environ. **88,** 453457 (2003).
20. F. G. Bass and I. M. Fuks, "Calculation of shadowing for wave scattering from a statistically rough surface," Sov. Radiophys. **7,** 101–112 (1964).
21. F. G. Bass and I. M. Fuks, "Wave Scattering from statistically rough surfaces," in *International Series in Natural Philosophy*, C. B. Vesecky and J. F. Vesecky, eds. (Pergamon, 1979).
22. P. I. Kuznetsov, V. L. Stratonovich, and V. I. Tikhonov, "The duration of random function overshoots," Sov. Phys. Tech. Phys. **24,** 103 (1954).
23. C. Bourlier, G. Berginc, and J. Saillard, "Monostatic and bistatic statistical shadowing functions from one-dimensional stationary randomly rough surface according to the observa-

tion length. I. Single scattering," Waves Random Media **12,** 145–174 (2002).
24. R. J. Wagner, "Shadowing of randomly rough surfaces," J. Opt. Soc. Am. **41,** 138–147 (1966).
25. B. G. Smith, "Lunar surface roughness, shadowing and thermal emission," J. Geophys. Res. **72,** 4059–4067 (1967).
26. B. G. Smith, "Geometrical shadowing of a random rough surface," IEEE Trans. Antennas Propag. **5,** 668–671 (1967).
27. P. Beckman, "Shadowing of random rough surfaces," IEEE Trans. Antennas Propag. **13,** 384–388 (1965).
28. C. Bourlier and G. Berginc, "Shadowing function with single reflection from anisotropic Gaussian rough surface. Application to Gaussian, Lorentzian and sea correlations," Waves Random Media **13,** 27–58 (2003).
29. R. A. Brokelman and T. Hagfors, "Note of the effect of shadowing on the backscattering of waves from a random rough surface," IEEE Trans. Antennas Propag. **14,** 621–627 (1967).
30. J. P. Theiler and B. G. Henderson, "Geometrical constraint on shadowing in rough surfaces," in *Infrared Spaceborne Remote Sensing V*, M. Strojnik and B. F. Andresen, eds., SPIE **3122,** 271–279 (1997).
31. G. M. Hale and M. R. Querry, "Optical constants of water in the 200-nm to 200-mm wavelength region," Appl. Opt. **12,** 555–563 (1973).
32. D. Friedman, "Infrared characteristics of ocean water (1.515 μ)," Appl. Opt. **8,** 2073–2078 (1969).
33. L. Pontier and C. Dechambenoy, "Détermination des constantes optiques de l'eau liquide entre 1 et 40 μ. Application au calcul de son pouvoir réflecteur et de son émissivté," Ann. Geophys. **22,** 633641 (1966).
34. D. J. Segelstein, "The complex refractive index of water," M.S. thesis (University of Missouri, 1981).
35. D. M. Wieliczka, S. Weng, and M. R. Querry, "Wedge shaped cell for highly absorbent liquids: infrared optical constants of water," Appl. Opt. **28,** 1714–1719 (1989).
36. R. W. Preisendorfer, "Albedos and glitter patterns of a wind-roughened sea surface," J. Phys. Oceanogr. **16,** 1293–1316 (1986).
37. C. Bourlier, G. Berginc, and J. Saillard, "Monostatic and bistatic statistical shadowing functions from one-dimensional stationary randomly rough surface according to the observation length. II. Multiple scattering," Waves Random Media **12,** 175–200 (2002).
38. A. Berk, L. S. Bernstein, and D. C. Robertson, "MODTRAN: a moderate resolution model for LOWTRAN7," AFGL Tech. Rep. GL-TR-89-0122 (U.S. Air Force Geophysics Laboratory, 1989).